



ORIGINAL RESEARCH ARTICLE

Behavior and Relationships between Residual Stresses and Mechanical Properties in Welded Joints of Aluminum Alloy AA5083-H116 Using Pulsed Gas Metal Arc Welding

Enrique Esteban Nieves-Nuñez, Jimmy Unfried-Silgado, Jaime Elías Torres-Salcedo, and Antonio J. Ramírez

Submitted: 1 June 2023 / Revised: 3 November 2023 / Accepted: 26 November 2023 / Published online: 28 December 2023

This work discusses several aspects of the weldability of AA5083-H116 butt-welded joints, using ER5183 filler material, automated GMAW-P process, and 80Ar19He1O₂ shielding gas. The used methodology included the characterization of base metal, the development of welded joints using two different heat inputs, the microhardness profiles analysis on the cross section of the welded joint, and the microstructural evolution using microscopy. The above-mentioned measurements were complemented with residual stress evaluation using the x-ray diffraction technique, together with analysis of transversal and longitudinal tensile tests of the welded joints. The obtained results in welded joints indicated that yield strength, ultimate tensile strength, and ductility behavior have been influenced by heat input compared to base metal and reported values for similar alloys. Residual stress results showed that both the weld metal and adjacent coarse grain zone were subjected to tensile stresses, while the refined grain zone (FGZ) and base metal adjacent to the FGZ were subjected to compressive stresses. Additionally, the magnitude of residual stresses was smaller than maximum tensile stresses, and its behavior was related to both heat input and mechanical properties along welding regions.

Keywords AA5083-H116 welded joints, aluminum, GMAW-P, mechanical testing, residual stress

1. Introduction

Al-Mg alloys (5xxx series) widely used in naval applications exhibit a high yield strength (S_y) in a range between 125 and 295 MPa. These values are similar to the S_y range of some naval steels, such as ASTM A131 and ASTM A36, which are between 235 and 250 MPa, respectively (Ref 1). Gas metal arc welding is a manufacturing process widely used to join aluminum alloys. In gas metal arc welding using pulsed transfer mode (GMAW-P), a

peak amperage is set above the spray transfer set point resulting in higher penetration (Ref 2). Meanwhile, a base amperage is set in the globular transfer range producing a cooling period. Combining these two currents produces a stable arc, with a controlled metal transfer, leading to higher deposition rates and lower heat input (Ref 3). Shielding pure gases commonly used in the GMAW process are argon (Ar) and helium (He). Ar-He and Ar-He-O₂ mixtures are used too. Frequent problems during the GMAW welding of aluminum alloys are related to pores presence caused by the solubility of excess free hydrogen during welding, vaporization of low melting alloying elements, and high cooling rates, as well as distortions and softening of the heat-affected zone (HAZ) (Ref 4, 5).

Plastic deformation and cold strain hardening of non-heat-treated aluminum alloys are associated with storage energy in the form of dislocations (Ref 6). The aforementioned phenomenon includes the multiplication of dislocations and the formation of subgrains in the deformed zones, which can be influenced by heating rates of the material during welding (Ref 7, 8). Due to strain hardening, there is an increase in the storage energy in the material due to the increase in the density of dislocations, which prevents the free sliding of dislocations, thereby increasing the strength and decreasing the ductility of the deformed alloy (Ref 8). During the welding process, the joint's constraints and the expansion and contraction of the welded metal, along with phase transformations caused by the heat input, lead to the generation of residual stresses (RSs) (Ref 9). The heat input from welding to these cold-formed alloys results in a rearrangement of dislocations, formation of subgrains, and new grains. This leads to a decrease in the mechanical resistance and hardness of the alloy. Furthermore, it causes a considerable decrease in the associated internal energy, facilitating the relief of RSs present in the welding (Ref 7, 10).

This invited article is part of a special topical issue of the *Journal of Materials Engineering and Performance* on Residual Stress Analysis: Measurement, Effects, and Control. The issue was organized by Rajan Bhambroo, Tenneco, Inc.; Lesley Frame, University of Connecticut; Andrew Payzant, Oak Ridge National Laboratory; and James Pineault, Proto Manufacturing on behalf of the ASM Residual Stress Technical Committee.

Enrique Esteban Nieves-Nuñez, Programa de Ingeniería Mecánica, Facultad de ingeniería, Grupo de investigación IMTEF, Universidad Autónoma del Caribe, 080020 Barranquilla, Colombia; **Jimmy Unfried-Silgado**, Departamento de Ingeniería Mecánica, Grupo de investigación ICT, Universidad de Córdoba, 230002 Montería, Colombia; **Jaime Elías Torres-Salcedo**, Programa de Doctorado en Ingeniería Mecánica, Universidad del Norte, 081001 Barranquilla, Colombia; and **Antonio J. Ramírez**, Welding Engineering Program, The Ohio State University Columbus, Columbus, OH. Contact e-mail: enrique.nieves@uac.edu.co.

RSs have an important effect on the service life of naval vessels. RSs can affect the structural strength in hull buckling and stresses in the deck superstructure, potentially causing cracking and brittle fractures under the intensity of the loads and waves undergone by the ship (Ref 11). The x-ray diffraction (XRD) method using the $\sin^2\psi$ technique is a non-destructive method commonly used to measure RSs in crystalline materials. The penetration depth of this technique is restricted to analyzing RSs close to the material's surface, usually in the range of 10-30 μm (Ref 12, 13). However, the penetration depth can be influenced by the angle of inclination θ , the angle of incidence (ψ) of the x-rays with respect to the surface of the material, the value of $\sin^2\psi$, the properties of the material, the type of radiation used, and the position of the Bragg's peak in 2θ (Ref 12, 14). When the depths of penetration increased (Ref 12), the RSs may differ from those measured at the surface due to stress distribution at different depths, material properties, and welding conditions. The penetration depth is increased as the ψ -tilt angle decreases (Ref 14, 15). Using a scanning range of ± 45 degrees for ψ -tilt angles and $\sin^2\psi$ values up to 0.5 provides greater sensitivity and precision for evaluating RSs at penetration depths beyond the sample's surface. However, working with narrower ranges might be convenient in cases of thin thicknesses or when reducing the measurement time for RSs is necessary. Nevertheless, this reduction in the scanning range might lead to sensitivity reduction and minor RSs' detection ability due to continuous variations of crystallographic orientation in the welded joint (Ref 13, 14). The accuracy level of the XRD- $\sin^2\psi$ residual stress measurement is associated with measurement errors determined by the instrument configuration, incorrect selection of the diffraction peak, nonlinear relationships in the $d - \sin^2\psi$ curve, the processing of data, likewise, by the coefficient (R^2) of the linear regression in the curve $d - \sin^2\psi$, and this in turn with the deviation value in the RS measurement, where high values of R^2 have low values of deviation (Ref 16, 17).

In this study, butt welding joints of AA5083-H116 alloy were produced using the GMAW-P process and 80Ar19He1O₂ as shielding gas, and varying heat input. Tensile tests were carried out in the transverse and longitudinal sections of the weld beads, additionally Vickers microhardness profiles were obtained, and the residual stress state was determined through x-ray diffraction tests. Additionally, the study was complemented with microstructure analysis of the welded joints, using optical microscopy. The goal of this work is to establish qualitative relationships among the tensile test results, microhardness profiles, residual stress state, and heat input of welding.

2. Materials and Methods

2.1 Determination of Alloy Identity

The identity of the AA5083-H116 alloy (Ref 18) (Table 1) was verified through chemical composition analysis using optical emission spectrometry, microstructural analysis by optical microscopy (OM), HV_{100g/10s} microhardness test, and tension testing.

Table 1 shows the chemical composition (wt.%) and mechanical properties of AA 5083-H116 alloy.

2.2 Welding

The butt welding joints were carried out using automated GMAW-P, in flat position (1G) and filler material ER5183 of diameter $\varnothing 1.2$ mm and shielding gas mixture 80Ar19He1O₂. A Railtrac[®] automatic system was used to control welding movements and speeds. The weld beads were obtained without gun oscillation. The following welding parameters were varied, adjusted, and set using the Optima[®] control unit: Start current I_b , peak current I_p , base current I_b , peak pulse time t_p , and pulse frequency f_p . Since it was not possible to measure the type of wave signal, for simplicity, it was supposed a rectangular wave signal for the calculation, see Eq 1.

$$I_m = \frac{I_b t_b + I_p t_p}{t_b + t_p} [\text{A}] \quad (\text{Eq 1})$$

Given both joint design and welding parameters, high and low heat inputs were calculated (Fig. 1a) maintaining at least a 10% difference between them. In total, four test plates were welded by each heat input, with dimensions of 300 mm \times 300 mm \times 4.6 mm (Fig. 1c). One plate was used for observation, and three for replica. The joint details and the location of the test specimens are shown in Fig. 1b and c, respectively. The specimens were extracted using CNC milling and abundant cooling.

2.3 Characterization of Microstructure and Mechanical Properties of the Welded Joints

The microstructure of welded joints was observed using optical microscopy (Olympus B51X), aiming to identify the different weld regions and morphological changes undergone by the different experienced thermal cycles. Etching of the microstructure of the welded joints was carried out with 10% H₃PO₄ phosphoric acid. The microhardness values of the welded regions were measured transversely along to the weld bead by applying a load of 100 g for 10 s with 0.15 mm of pitch in accordance with ASTM-E384 guidelines (Ref 19). For the transverse tensile strength analysis were tested four (4) reduced section tensile specimens by each thermal condition (Fig. 2) according to AWS D1.2 (Ref 20). The tensile tests were developed in a SHIMADZU[®] UH-100A universal testing machine with a head speed of 4 mm/min.

The specimens for the longitudinal tensile test were located and scaled according to ASTM B557-15, using a total of 4 replicates for each heat input and welding region (Fig. 3a and b), and the dimensions of the specimen are provided in Fig. 3(c) (Ref 21). The location of the longitudinal tensile test was based on the analysis of microstructure and hardness evolution and named in the following manner: multizone (contains elements of the partially melted zone (PMZ), weld metal (WM), and coarse grain zone (CGZ)), CGZ, fine grain zone (FGZ), and base metal (BM). The obtained results were analyzed as a qualitative indicator, based on how each weld region is thermally affected, understanding that during the cutting and preparation of the specimens, they undergo deformations and relief of residual stresses that could affect them.

2.4 Welded Joint Residual Stress Measurements

Residual stress tests were developed using x-ray diffraction equipment, X'PERT PRO[®] by PANalytical. The state of RSs was measured for each weld region in both transverse and longitudinal directions using points distributed parallel and

Table 1 Chemical composition (wt.%) and mechanical properties of AA 5083-H116 alloy

Alloy	Si	Fe	Cu	Mn	Mg	Cr	Zn	Ti	Other elements	Al
5083-H116	0.02	0.24	0.18	0.42	4.02	0.06	0.01	0.06	0.05	Balance
Yield strength \bar{S}_y, MPa	Ultimate tensile strength \bar{S}_u, MPa				Elongation $\bar{E}2in$, %				Microhardness \bar{HV}	
243	337.5				12.3				96.3	

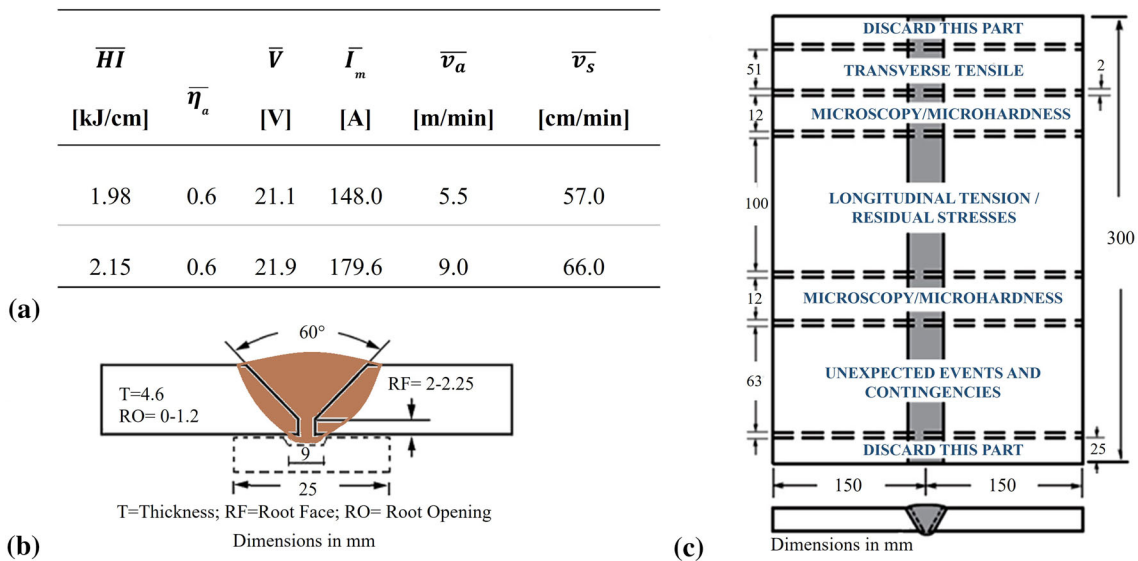


Fig. 1 (a) Welding parameters. (b) Joint design. (c) Location of the test specimens, units in mm. HI = Heat input, I_m = average current, η_a = process efficiency, V = voltage, v_a = wire feed speed, and v_s = welding speed

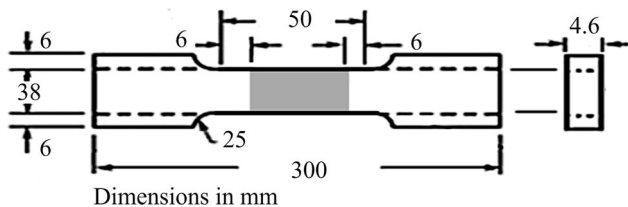


Fig. 2 Geometry of the test specimen for transverse tensile testing (Ref 20)

perpendicular to the weld bead (Fig. 4). To define the spacing and diffraction points, the following considerations were made to ensure that the x-ray beam was directed onto each identified weld region in the microstructure analysis. The spacing was varied along the length of the weld bead, and the size of the region diffracted by the incident x-ray on the sample was approximately $1.5 \times 1.5 \text{ mm}^2$. The diffraction points for the measurement of RSs, distributed in the direction perpendicular to the weld bead, are located at distances from the weld center as follows: weld metal (0 mm), the ZGG (6.3 mm), ZGF (11.7 mm), and BM (30 mm and 40 mm). The diffraction points for the measurement of the RSs, distributed in the longitudinal direction and parallel to the weld bead, are located at the following distances from the center of the welded plate: 0 mm, 10 mm, 20 mm, - 10 mm. The surface of the weld

bead was polished to be smooth, clean, and free of oxides. The method used to measure the RSs is the $\sin^2\psi$ method (Ref 13). The radiation used for this test was Co tube radiation with wavelengths $K\alpha_1$ (A) = 1.789010 and $K\alpha_1$ (A) = 1.792900 and a scanning step size of 0.02°.

Five x-ray diffraction scans in continuous mode were performed, each with a different inclination angle (ψ) of 0°, 11.24°, 16.00°, 19.73°, and 22.95°, and 2θ angle in the scan range from 96.95° to 101.45°, to measure the diffraction peaks and interplanar spacings for each ψ value necessary for a better characterization and analysis of RSs data. In the different diffraction points and scans conducted, the Bragg angle 2θ varied approximately between 99.1° and 99.3°. The determination of the RSs value was carried out using the X'Pert Stress module of the X'Pert HighScore® software from the equipment. The stress data were processed using the method of unidirectional stress analysis. As elastic constants of the material for calculating the interplanar distance d (Å) defined by Bragg's law, the elastic modulus $E = 71 \text{ MPa}$ and the Poisson's ratio $\nu = 0.33$ were used. For aluminum alloys, the penetration depth achieved in the range of $\sin^2\psi < 0.2$, using Co radiation, is approximately $20 \mu\text{m}$, as reported in the literature (Ref 13). Supported by software, the diffraction peaks were analyzed (Fig. 5a), and then, the RS value and associated deviation were calculated using the interplanar spacing graph $d(\text{Å})-\sin^2\psi$ (Fig. 5b) by carefully adjusting the slope associated

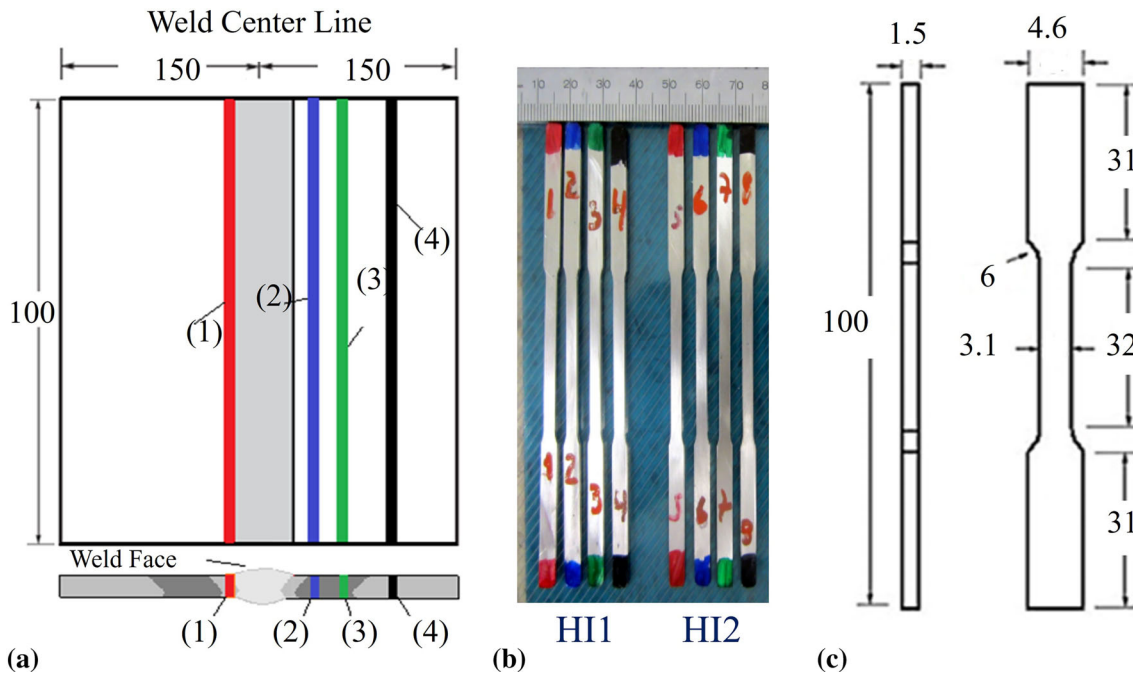


Fig. 3 Position and geometry of longitudinal stress specimens. (a) Position for removal. (b) Identification by welding region, 1-Red = Multizone, 2-Blue = ZGG, 3-Green = ZGF, 4-Black = MB. (c) Geometry of the specimen. HI1 = 1.98 [kJ/cm]. HI2 = 2.15 [kJ/cm]. Dimensions in mm (Color figure online)

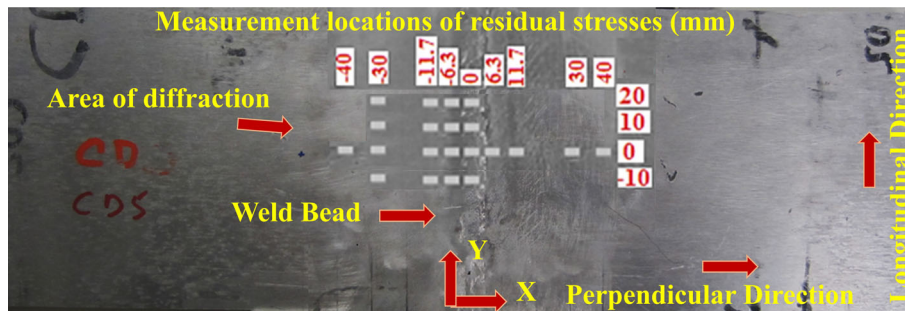


Fig. 4 Distribution of locations along the weld bead for the measurement of residual stresses

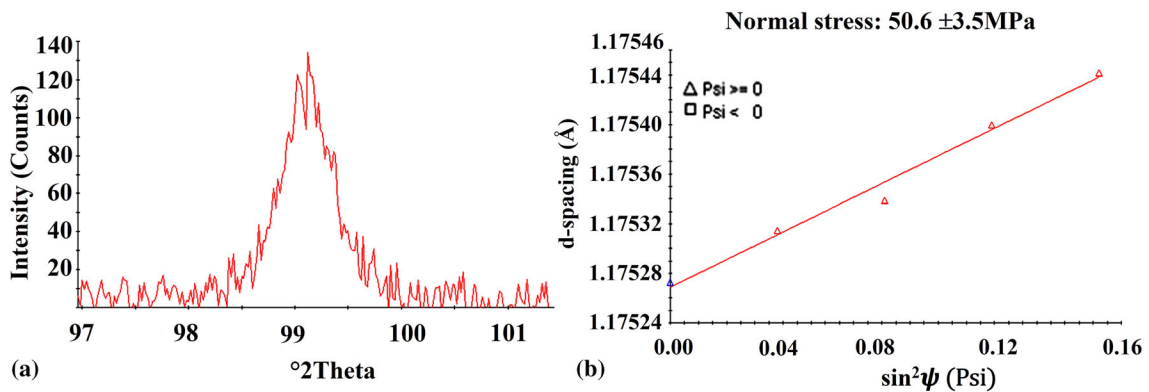


Fig. 5 Estimation of RS using the $\sin^2\psi$ method. (a) Diffraction peak 2 θ . (b) Interplanar spacing graph $d(\text{\AA})-\sin^2\psi$

with the linear regression of the curve. Finally, the RSs data obtained are imported into data analysis software and plotted, aiming to display the distribution of the residual stress state in each welded joint.

3. Results and Discussion

3.1 Microstructure and Hardness Evolution

Results of microstructural analysis of the AA5083-H116 aluminum alloy welded joint under the optical microscopy technique showed the welding regions identified as coarse grain zone—CGZ, mixed grain zone—MGZ, and fine grain zone—FGZ (Fig. 6).

The result of the distribution of Vickers microhardness measurements in the AA5083-H116 welded joint shows that there is a uniform softening along of HAZ regions of the welded joint, obtaining an average hardness of 73 HV corresponding to the other weld zones (Fig. 7a). This softening is more pronounced between the fusion zone and the GFZ vicinities, showing a decrease from 96 HV of the base metal to 62 HV (Fig. 7b), probably produced by recrystallization effects.

3.2 Behavior of Strength and Ductility Indicators from Transverse Tension Tests

Results of transverse tension tests are shown in Fig. 8.

Figure 8(a) shows the behavior of average values of S_y and S_u in function of different studied thermal inputs. It can be observed that S_y and S_u values decreased compared to the base metal by 26% and 32%, respectively. When comparing the values experimentally obtained in this work with those reported by Ilman et al. (Ref 22), for AA5083-H116 welded joints using the GMAW process, ER5346 filler material, and argon shielding gas, increasing by 30% and 31% was observed, respectively. Similarly, When comparing obtained experimental values reported by Dutra et al. (Ref 23), for AA5083-H116 welded joints using the GMAW with cold metal transfer process, ER5183 filler material, and argon shielding gas, S_y values are higher by 18% and the S_u values are lower by 22%, respectively. Regarding the percentage of elongation values (Fig. 8b), no statistical differences are observed among the

values experimentally obtained for the different heat inputs, while compared to base metal those decreased by approximately 43%.

3.3 Longitudinal Tensile Test Results Analysis

The results of longitudinal tensile tests for yield and ultimate strength analysis are shown in Fig. 9.

Figure 9(a) shows the effect of heat input on the yield strength (S_y), decreasing 53% and 42% compared to the base metal (BM) in the multizone (PMZ-multizone) and the coarse-grained zone (CGZ), respectively. The highest S_y values were reached in the fine-grained zone (FGZ), which, however, decreased by 19% compared to the base metal. As for the ultimate strength (S_u) (Fig. 9b), the results show that there are no statistical differences between the values obtained for the different heat inputs.

3.4 Residual Stress Results Analysis

The results of the residual stress analysis are shown in Fig. 10. The FGZ and the base metal adjacent to the FGZ are subjected to compressive residual stresses (between -25 MPa and -10 MPa), which are smaller in magnitude than the higher tensile residual stresses (30 MPa to 70 MPa). It is remarkable that residual stresses converge to zero, for the two studied heat inputs, at approximately 9.5 mm and 10 mm, respectively, from the welded joint center. The above-mentioned suggests that this point is the place where the energy accumulated by deformation has probably been fully released and recrystallization begins.

It can be observed from Fig. 10(a) that the maximum value of residual stresses in the longitudinal direction in the weld metal (92.9 MPa) is higher than the residual stresses in the transverse direction (36.5 MPa) in the same region. Figure 10(b) shows the residual stresses in the longitudinal direction (maximum average value 65.1 MPa), which is higher than the higher average residual stresses in the transverse direction (39.8 MPa) in the same region. For both heat inputs, the behavior of RSs values shows that the regions of the weld metal and adjacent until CGZ are under tensile stresses, and the other regions are under compression stress. Average values of RS at the longitudinal direction are greater than those in the

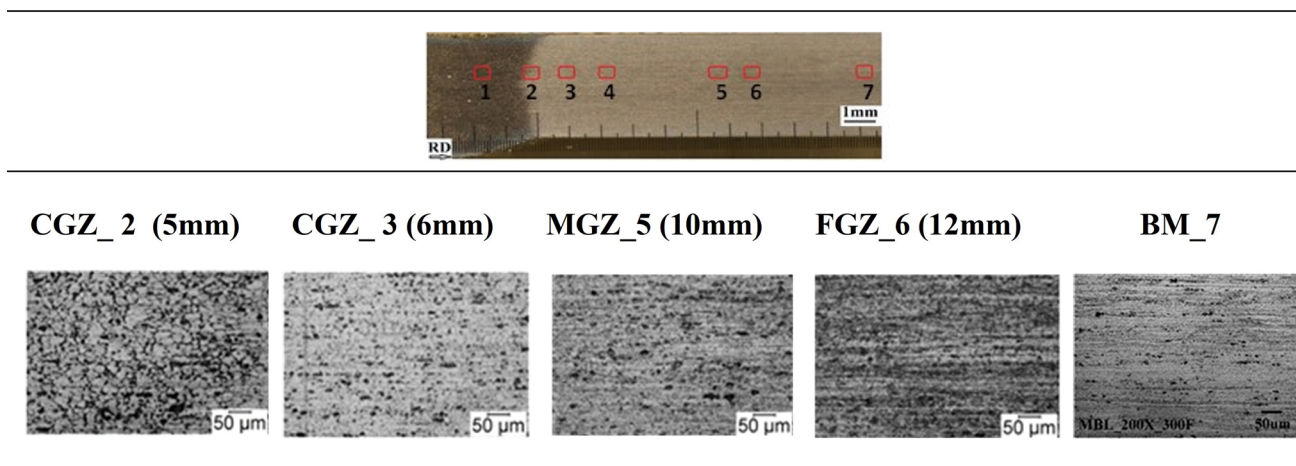


Fig. 6 Microstructural evolution in the weld regions. 10% H_3PO_4 etching. MO images. Magnification 200X. Average HI = 1,98 [kJ/cm]. (xx) = Distance to the weld center in millimeters

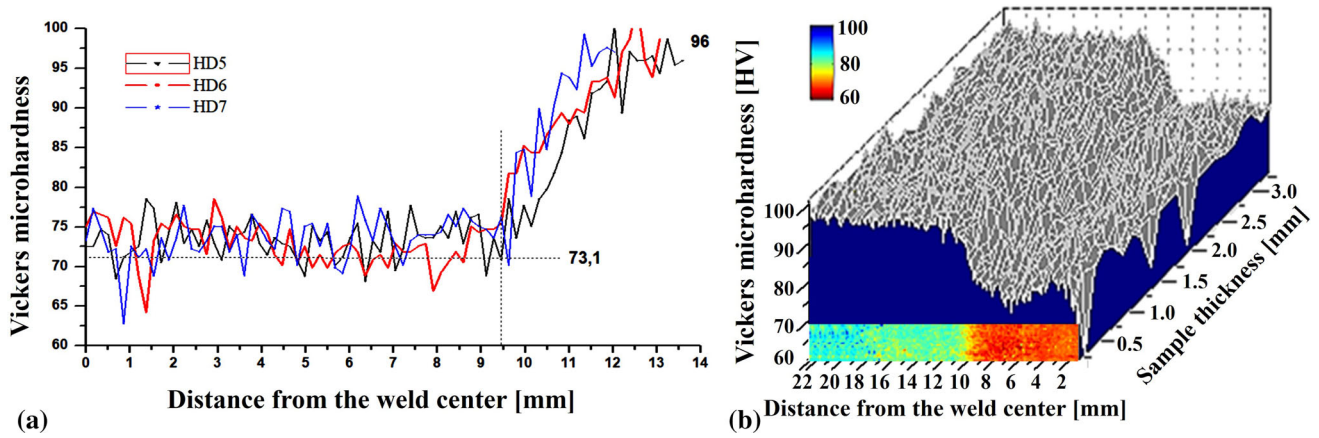


Fig. 7 Microhardness measurements: (a) Cross section. (b) Microhardness map. Average HI = 1.98 [kJ/cm]

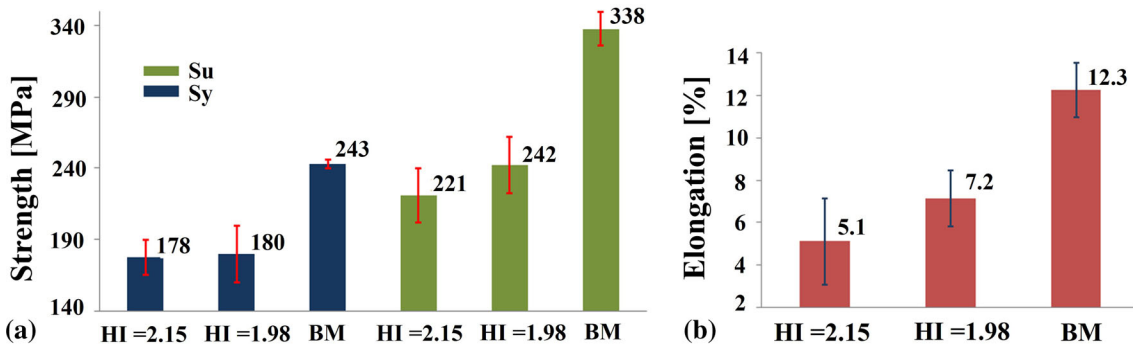


Fig. 8 (a) Indicators of transverse strength. (b) Indicators of transverse elongation. Average HI in [kJ/cm]

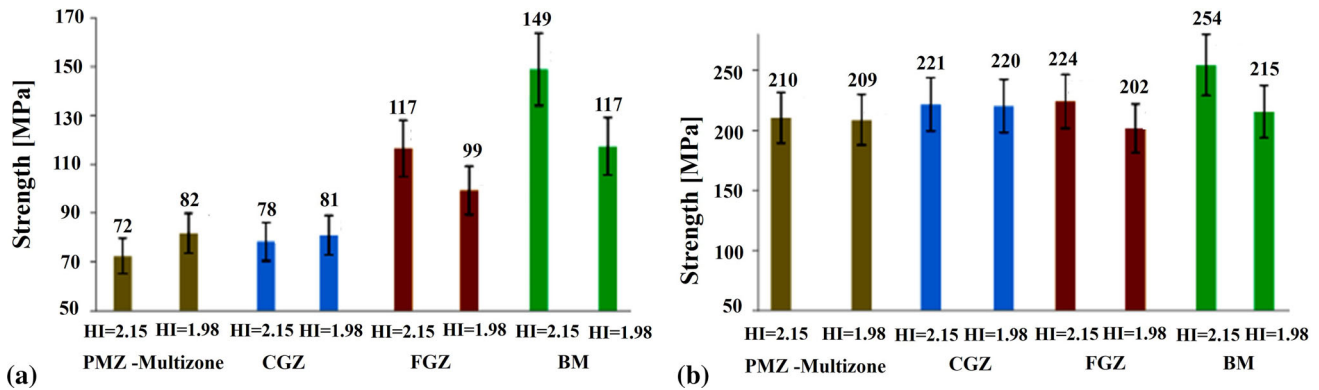


Fig. 9 Longitudinal indicators of strength in function of heat input. (a) Yield strength (Sy). (b) Ultimate strength (Su). Error bars are set at 10%. Average HI in [kJ/cm]

transverse direction, which is consistent with results of Lu et al. (Ref 24). Additionally, it is observed that the longitudinal RS (σ_{yy}) is greater for the welded joints with 1.98 [kJ/cm] heat input. Results of RS analysis at points distributed in the parallel to longitudinal direction of the weld bead for each heat input are shown in Fig. 11. According to abovementioned results, along of welding bead and toward the middle part of the plate are observed tensile RSs, which decrease toward the plate's ends (Ref 25). The behavior of the RS values in different welding regions compared with those of the perpendicular direction is similar. Tensile RSs are observed between the weld

metal (WM) and the CGZ, while compressive RSs were observed in the FGZ and regions near the base metal (BM).

4. Conclusions

Analysis of the results shows that the yield stress is sensitive to heat input. The ultimate strength is not very sensitive to changes in heat input, reflecting a slight uniformity between the values obtained, with a margin of loss of approximately 30% compared to the base metal. When comparing the results of the

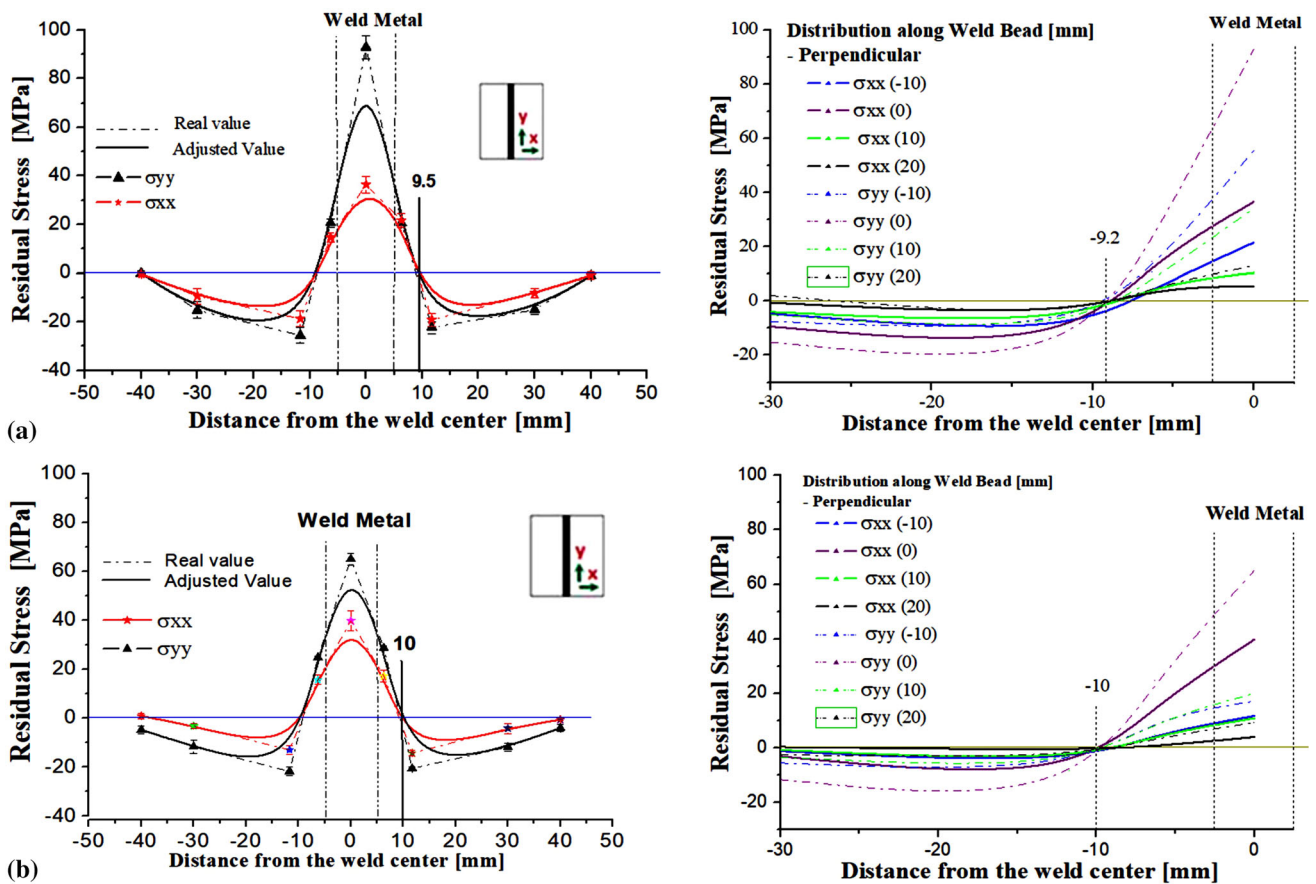


Fig. 10 Residual stress distribution perpendicular to the welding direction. (a) Average HI = 1.98 [kJ/cm]. (b) Average HI = 2.15 [kJ/cm]

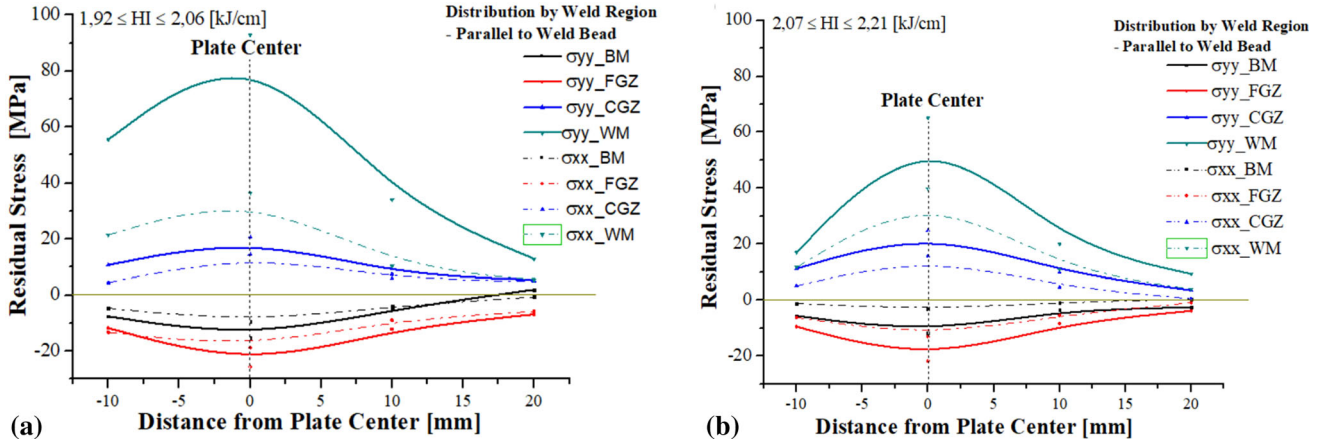


Fig. 11 Residual stress distribution parallel to the welding direction. (a) Average HI = 1.98 [kJ/cm]. (b) Average HI = 2.15 [kJ/cm]

elongation percentage with the values of the base metal, reduction of ductility of approximately 43% is evidenced, compared to the base metal. The analysis of the results on the longitudinal tensile strength indicators shows that the weld region with the best strength indicators is the FGZ and especially with average heat input of 2.15 [kJ/cm]. Residual stresses analysis showed that the weld metal and the coarse-grained zone (CGZ) are subjected to tensile residual stresses. On the other hand, the fine-grained zone (FGZ) and the base metal (BM) adjacent to the FGZ are subjected to compressive

stresses. Values of compressive residual stresses were smaller in magnitude than the tensile residual stresses.

Acknowledgments

The authors would like to gratitude to Universidad del Norte, Universidad Autónoma del Caribe, COTECMAR, SENA- Centro Colombo Alemán, and CNPEM/ABTLuS as well as its Laboratório Nacional de Nanotecnologia - LNNano in Campinas, Brazil, for their financial and logistical support to the project.

References

1. M.A. Wahid, A.N. Siddiquee, and Z.A. Khan, Aluminum Alloys in Marine Construction: Characteristics, Application, and Problems from a Fabrication Viewpoint, *Marine Syst. Ocean Technol.*, 2020, **15**, p 70–80.
2. A. Hadadzadeh, M.M. Ghaznavi, and A.H. Kokabi, HAZ Softening Behavior of Strain-Hardened Al-6.7Mg Alloy Welded by GMAW and Pulsed GMAW Processes, *Int. J. Adv. Manuf. Technol.*, 2017, **92**, p 2255–2265.
3. E. Aldalur, A. Suárez, and F. Veiga, Metal Transfer Modes for Wire Arc Additive Manufacturing Al-Mg alloys: Influence of Heat Input in Microstructure and Porosity, *J. Mater. Process. Technol.*, 2021, **297**, p 117271.
4. R.P. Verma, K. Pandey, K. András, R. Khargotra, and T. Singh, Difficulties and Redressal in Joining of Aluminium Alloys by GMA and GTA Welding: A Review, *J. Mater. Res. Technol.*, 2023, **23**, p 2576–2586.
5. R.D. Ardika, T. Triyono, and N. Muhayat, A Review Porosity in Aluminum Welding, *Procedia Struct. Integr.*, 2021, **33**, p 171–180.
6. W. Woo, L. Balogh, T. Ungár, H. Choo, and Z. Feng, Grain Structure and Dislocation Density Measurements in a Friction-Stir Welded Aluminum Alloy Using X-ray Peak Profile Analysis, *Mater. Sci. Eng. A*, 2008, **498**(1–2), p 308–313.
7. A. F. Padilha nad F. Siciliano Jr., Encruamento, recristalização, crescimento de grao e textura, Sao Paulo: ABM-Asociação Brasileira de Metalurgia e Materiais, 2005. (In Portuguese)
8. F. J. Humphreys and M. Hatherly, Recrystallization and Related Annealing Phenomena, Oxford: Elsevier Ltd., 2004
9. M.-S. Yi and P. Joo-Shin, Study of Heat Source Model and Residual Stress Caused by Welding in GMAW of Al Alloy, *Metals*, 2022, **12**(6), p 891.
10. X. Lei, R.E. Sanders, X. Yang, F. Lin, and D. Juul Jensen, Quantitative Comparison of the Recrystallization Kinetics of Two Industrially Processed 5xxx Aluminum Alloys, *Metall. Mater. Trans. A*, 2021, **52**, p 4827–4840.
11. D. Casassola Gonçalves, M. Campos Martins, and M.P. Cindra Fonseca, Estudo Experimental e Numérico de Tensões Residuais em Juntas Soldadas com e sem Restrição, *Soldagem & Inspeção*, 2017, **22**(2), p 147–162.
12. J. Guo, H. Fu, B. Pan, and R. Kang, Recent Progress of Residual Stress Measurement Methods: A Review, *Chin. J. Aeron.*, 2021, **34**(2), p 54–78.
13. M. E. Fitzpatrick, A. T. Fry, P. Holdway, F. A. Kandil, J. Shackleton, and L. Suominen, Measurement Good Practice Guide No. 52 Determination of Residual Stresses by X-ray Diffraction - Issue 2, United Kingdom: National Physical Laboratory, 2005
14. C. E. Murray and I. C. Noyan, Applied and Residual Stress Determination Using X-ray Diffraction, de *Practical Residual Stress Measurement Methods*, G. S. Schajer, Ed., West Sussex, Wiley, 2013, 139-162
15. A. Kumar, U. Welzel, and J. Mittemeijer, A Method for the Non-Destructive Analysis of Gradients of Mechanical Stresses by X-ray Diffraction Measurements at Fixed Penetration/Information Depths, *J. Appl. Crystall.*, 2006, **39**(5), p 633–646.
16. Q. Luo and A. Jones, High-Precision Determination of Residual Stress of Polycrystalline Coatings Using Optimised XRD-sin 2ψ Technique, *Surf. Coat. Technol.*, 2010, **205**, p 1403–1408.
17. Q. Luo, A Modified X-ray Diffraction Method to Measure Residual Normal and Shear Stresses of Machined Surfaces, *Int. J. Adv. Manuf. Technol.*, 2022, **119**(5–6), p 3595–3606.
18. ASTM International, ASTM B928/B928M-15 Standard Specification for High Magnesium Aluminum-Alloy Products for Marine Service and Similar Environments, ASTM International, West Conshohocke, 2015
19. ASTM International, E384–17. Standard Test Method for Knoop and Vickers Hardness of Materials, West Conshohocken: ASTM International, 2017
20. American Welding Society -AWS, *AWS D1.2/D1.2M:2014 Structural Welding Code - Aluminum*, Miami, Florida: American Welding Society, 2014
21. ASTM International, B557-15. Standard Test Methods for Tension Testing Wrought and Cast Aluminum- and Magnesium-Alloy Product,» ASTM International, West Conshohocken, 2015
22. M. Ilman, R. Sriwijaya, M.R. Muslih, and N.A. Triwibowo, Strength and Fatigue Crack Growth Behaviours of Metal Inert Gas AA5083-H116 Welded Joints Under in-Process Vibrational Treatment, *J. Manuf. Processes*, 2020, **59**, p 727–738.
23. J.C. Dutra, R. H. G. e Silva, B. M. Savi, C. Marques, and O. E. Alarcon, Metallurgical Characterization of the 5083H116 Aluminum Alloy Welded with the Cold Metal Transfer Process and Two Different Wire-Electrodes (5183 and 5087), *Weld. World*, 2015, **59**, p 797–807.
24. Y. Lu, S. Zhu, Z. Zhao, T. Chen, and J. Zeng, Numerical Simulation of Residual Stresses in aluminum Alloy Welded Joints, *J. Manuf. Process.*, 2020, **50**, p 380–393.
25. S. Kou, *Welding Metallurgy*, Wiley, New Jersey, 2020

Publisher's Note Springer Nature remains neutral with regard to jurisdictional claims in published maps and institutional affiliations.

Springer Nature or its licensor (e.g. a society or other partner) holds exclusive rights to this article under a publishing agreement with the author(s) or other rightsholder(s); author self-archiving of the accepted manuscript version of this article is solely governed by the terms of such publishing agreement and applicable law.